








Multifrequency Neural Network-based Wave Inversion in MR Elastography

Héloïse Bustin^{1,2}, Tom Meyer², Jakob Jordan², Lars Walczak^{1,2,3}, Heiko Tzschätzsch², Ingolf Sack^{2*}, and Anja Hennemuth^{1,2,3,4*}

¹ Deutsches Herzzentrum der Charité, Institute of Computer-assisted Cardiovascular Medicine, Augustenburger Platz 1, 13353 Berlin, Germany

² Charité – Universitätsmedizin Berlin, corporate member of Freie Universität Berlin and Humboldt Universität zu Berlin, Charitéplatz 1, 10117 Berlin, Germany

³ Fraunhofer MEVIS, Berlin, Germany

⁴ DZHK (German Centre for Cardiovascular Research), Berlin, Germany
`heloise.bustin@charite.de`

Abstract. Magnetic Resonance Elastography (MRE) is a non-invasive imaging modality quantifying soft tissue stiffness. The reconstruction of stiffness maps is based on solutions of an inverse problem, which poses challenges in balancing accuracy, computational resources, and robustness. To stabilize the reconstruction, many inversion techniques, and most recently neural network-based inversion techniques, have explored multifrequency acquisition and reconstruction. However, these techniques typically perform separate single-frequency inversions followed by multifrequency aggregation. In this work, we propose a fully multifrequency neural network-based inversion trained on synthetically generated data that directly incorporates the relationship between multifrequency acquisitions, assuming a viscoelastic material model. Our proposed approach provides flexibility with respect to the acquisition frequencies, ensuring its practical applicability in the clinical and research setting. We evaluated our method using finite element simulations and *in vivo* abdominal MRE datasets, achieving increased accuracy and providing a more reliable and effective solution for MRE-based tissue characterization than standard reconstruction approaches.

Keywords: Magnetic resonance elastography · Multifrequency inversion · Deep learning

1 Introduction

Magnetic Resonance Elastography (MRE) is a non-invasive imaging modality quantifying soft tissue stiffness by imaging the propagation of mechanical waves through the body [17]. Tissue stiffness is a key biomarker in many pathological conditions and is increasingly used in applications such as staging liver fibrosis [14]. The acquisition process involves placing an actuator on the patient

* These authors contributed equally to this work.

producing mechanical vibrations that induce acoustic waves (Figure 1). Motion-encoding gradients synchronized with the vibrations encode tissue displacements into the phase of the complex MR signal. This process is repeated to obtain 3D displacement wavefields at different vibration frequencies [11,12].

MRE involves solving an inverse problem to reconstruct either the shear modulus or the shear wave speed (SWS) as a surrogate for tissue stiffness from acquired wave displacement data (Figure 1). Solutions to the inverse problem are ill-posed due to unknown boundary conditions as well as the presence of noise and compression waves in the acquired wavefields. While a variety of methods have been developed [4,5], balancing accuracy, computational cost, and robustness remains a challenge. Two prominent inversion methods used in research and clinical practice are local frequency estimation (LFE) [9] and the phase-gradient inversion method known as k-MDEV [21]. Both methods are publicly available for server-based MRE data processing at <https://bioqic-apps.charite.de> [13].

In recent years, neural networks have shown promising results in MRE wave inversion [15,19,20,10,16,3]. A key challenge is the lack of ground truth for training machine learning models that can translate to clinical practice. To address this, several studies have explored training on small image patches of synthetically generated data [15,19,20,10,3], including TWENN [10] and ElastoNet [3]. During inference, small image patches are extracted from the acquired image, iteratively reconstructing it, a strategy that has been shown to generalize well to *in vivo* data. Many of these machine learning-based methods rely on multifrequency acquisitions to stabilize the inversion process but are trained assuming single-frequency input data. The predicted stiffness maps for each frequency are reconstructed separately and then aggregated. Such an approach may not fully leverage the information available in multifrequency data. We hypothesize that training a neural network directly on multifrequency data would lead to a more stable inversion process and, therefore, to more accurate stiffness maps.

In this work, we introduce the first fully multifrequency neural network-based inversion method in MRE (MF-ElastoNet), which integrates multiple acquisitions at different frequencies as direct inputs to the model. The model is designed to be flexible in both the number and values of acquired frequencies to facilitate its use in research and clinical settings. We assume a viscoelastic material model for the tissue’s frequency response to ensure its applicability to a wide variety of soft tissue types. We evaluate our method on finite element method (FEM) simulations and *in vivo* abdominal datasets, demonstrating the accuracy and anatomical detail of the SWS maps produced.

2 Method

2.1 Neural network-based wave inversion

Training a neural network to learn the inverse operation of reconstructing the SWS from the acquired displacement wavefields involved generating a synthetic dataset of wave displacement and shear wavelength pairs (\mathbf{u}, λ_s) . The shear

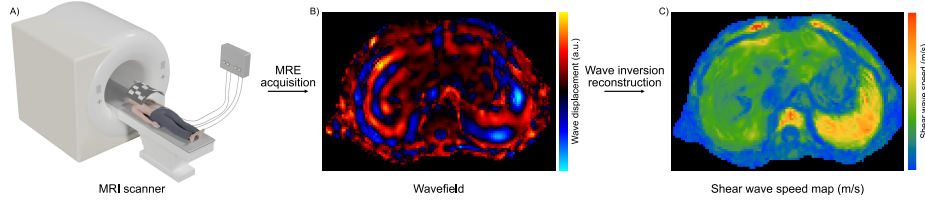


Fig. 1. MRE acquisition pipeline. A) MRI acquisition using actuators vibrating at a selected frequency. B) Wavefield acquired through encoding the wave displacements in the phase of the MR signal. C) SWS (shear wave speed) map obtained following the wave inversion reconstruction used as a proxy for the tissue stiffness.

wavelength, defined in pixel numbers, served as a proxy for the SWS to ensure that the data are independent of the image resolution Δr and vibration frequency f . The relationship is given by $c = \Delta r \cdot f \cdot \lambda_s$, where c is the SWS. For a multifrequency acquisition with N frequencies, we have $\lambda_s = (\lambda_1, \dots, \lambda_N)$. The following minimization problem was then solved:

$$\hat{W} = \arg \min_W D(\lambda_s, G(\mathbf{u}, W)) \quad (1)$$

where $D(\cdot, \cdot)$ is the cost function to be minimized by the neural network $G(\mathbf{u}, W)$ parameterized by weights W [8].

2.2 Training data generation

We used a linear isotropic viscoelastic material model to represent biological soft tissue [18,7], assuming local homogeneity [15,10,3]. Small patches of wave images were generated for each frequency and displacement component acquisition with the complex wave displacement \mathbf{u} at a given location \mathbf{r} expressed as a superposition of shear waves, compression waves, and noise:

$$\begin{aligned} \mathbf{u}(\mathbf{r}) = & \sum_{j=1}^{N_s} a_{sj} e^{-i\left(\left(\frac{2\pi}{\lambda_{sj}} - i\frac{1}{\delta_{sj}}\right)\mathbf{n}(d, \theta, \varphi) \cdot \mathbf{r}_j + \phi_{sj}\right)} \\ & + \sum_{j=1}^{N_c} a_{cj} e^{-i\left(\left(\frac{2\pi}{\lambda_{cj}} - i\frac{1}{\delta_{cj}}\right)\mathbf{n}(d, \theta, \varphi) \cdot \mathbf{r}_j + \phi_{cj}\right)} + \eta(\mathbf{r}) \end{aligned} \quad (2)$$

where a_s , a_c , ϕ_s , and ϕ_c are the amplitudes and phases of the shear and compression waves. N_s and N_c are the numbers of superimposed shear and compression wave sources in 3D space. \mathbf{n} is the normal vector for each point source in polar coordinates (d, θ, φ) . λ_s , λ_c , δ_s , and δ_c are the wavelengths and penetration lengths of the shear and compression waves in pixel numbers. $\eta(\mathbf{r})$ is zero-mean Gaussian noise applied to the real and imaginary parts of the wavefield. The parameter ranges were chosen as in [3].

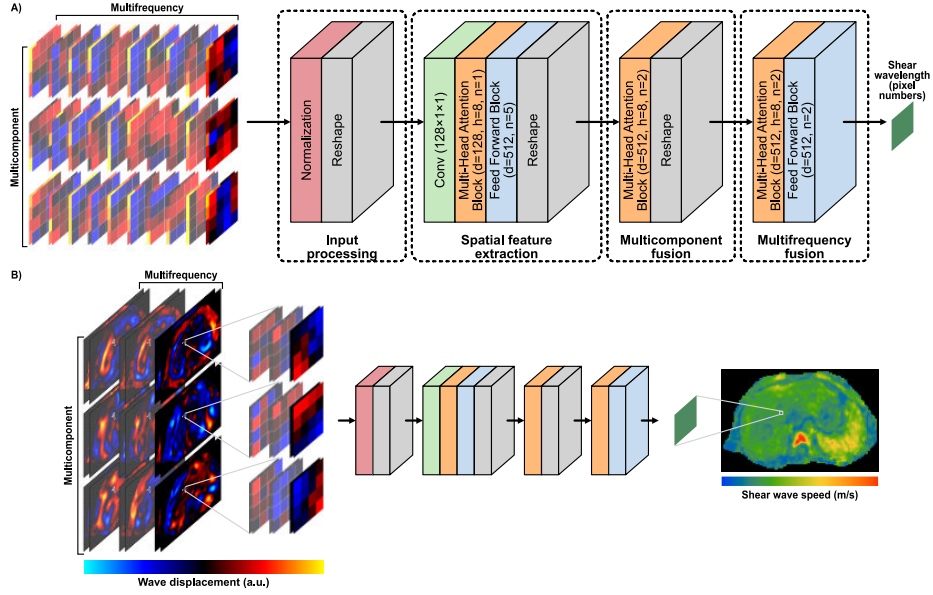


Fig. 2. A) Neural network training: Multifrequency and multicomponent complex-valued 4×4 wave displacement patches and associated shear wavelength pairs are synthetically generated for training. In the multi-head attention blocks, d is the embedded dimension, h the number of heads, and n the number of blocks. In the feed-forward blocks, d is the number of features and n the number of blocks. B) Inference: 4×4 patches are extracted from the real and imaginary parts of the acquired wavefield for every frequency and component, reconstructing the SWS (shear wave speed) maps.

2.3 Multifrequency modeling

Several conditions were set to model the tissue's frequency response while ensuring the applicability of the method to a wide variety of acquisition protocols and tissue types.

Number of acquired frequencies. This number is unknown a priori and can vary significantly depending on the imaging protocol. To capture the vast majority of clinical and research use cases, the number of acquisition frequencies was uniformly sampled between one and ten for each sample.

Material model assumptions. We assumed that the target material follows a linear isotropic viscoelastic model, which captures the mechanical behavior of a wide variety of soft biological tissues [7]. The SWS in such tissues has been widely observed to exhibit a power-law dependence on frequency, given by $c \propto f^{\frac{\alpha}{2}}$ with $0 \leq \alpha \leq 1$, where the extremes correspond to ideal elastic and viscous behaviors, respectively [18, 7]. For $\alpha = 0$, c is constant, and the wavelength

follows $\lambda(f) = \frac{c}{f}$. For $\alpha = 1$, $c(f) \propto \sqrt{f}$, and the wavelength follows $\lambda(f) \propto \frac{1}{\sqrt{f}}$. This formulation allowed us to constrain the generated wavelengths based only on the ratios between acquired frequencies and not specific values.

1. *Wavelength constraint*: We assumed N acquisition frequencies and that the associated wavelengths fall within a training range $[\lambda_{\min}, \lambda_{\max}]$. For a given acquisition n , we constrained the corresponding wavelength such that:

$$\forall n \in [1; N], \lambda_{\min} \leq \lambda_1 \leq \lambda_n \leq \lambda_N \leq \lambda_{\max} \quad (3)$$

2. *Power-law constraint*: From the material model, we derived constraints on the wavelengths and on the distance between the wavelengths associated to neighboring acquisition frequencies for the synthetic data generation:

$$\forall n \in [1, N], \lambda_{\min} \sqrt{\frac{f_1}{f_n}} \leq \lambda_n \leq \lambda_{\max} \sqrt{\frac{f_N}{f_n}} \quad (4)$$

$$\forall n \in [1, N-1], \lambda_{\min} \left(\sqrt{\frac{f_n}{f_{n+1}}} - 1 \right) \leq \lambda_{n+1} - \lambda_n \leq \lambda_{\max} \left(\frac{f_n}{f_{n+1}} - 1 \right) \quad (5)$$

3. *Penetration length constraint*: To ensure physically plausible data, the penetration length δ associated to a given wavelength λ must follow:

$$\delta \leq \frac{\lambda}{2\pi} \quad (6)$$

Acquisition frequencies. The acquisition frequencies used in MRE vary depending on the application. In human applications, frequencies generally range from 5 to 100 Hz, with a step size of 5 or 10 Hz. In research protocols, particularly in small animals, acquisitions extend to frequencies in the range of 1000 Hz with step sizes of 100 Hz.

The multifrequency material model detailed above only sets constraints based on the relative ratios of the frequencies rather than their absolute values. Therefore, the training dataset was generated to cover a range of frequency ratios from 0.5 to 0.95 instead of specific frequencies, ensuring the applicability of the model across various acquisition protocols.

2.4 Neural network architecture

Each input to the neural network consisted of 4×4 complex-valued wave patches, with the real and imaginary parts stacked as channels for the three displacement components and each acquisition frequency. The complex-valued patches were normalized by the average of their modulus.

The neural network architecture, displayed in Figure 2, followed a three-step hierarchical structure, each consisting of a vision transformer processing information at the spatial, displacement components, and frequency levels. In the spatial

feature extraction block, attention was applied along the stacked pixel dimension. In the multicomponent fusion block, it was applied along the displacement direction dimension. In the multifrequency fusion block, the frequency dimension was padded to the maximum size of ten acquisition frequencies, accommodating the variable input size. Attention was then applied along the frequency dimension, with masking corresponding to the padding.

A feed-forward block followed the multi-head attention layer in the spatial feature extraction and multifrequency fusion blocks. It consisted respectively of five and two feed-forward layers interspersed with layer normalization.

The GeLU activation function was used throughout the network, and Softplus was used as output activation to ensure physically realistic values.

2.5 Image reconstruction

For each acquired frequency and displacement component, 4×4 patches were extracted from the acquired wavefield. The corresponding estimated SWS \hat{c} was then reconstructed from the estimated shear wavelength $\hat{\lambda}_s$ in pixel numbers using the trained model:

$$\hat{c} = \Delta r \cdot f \cdot \hat{\lambda}_s = \Delta r \cdot f \cdot G(\mathbf{u}, W) \quad (7)$$

All reconstructed values were assembled to form the final SWS map. The training and inference reconstruction processes are illustrated in Figure 2.

3 Experiments

3.1 Setup

Data. All datasets used are publicly available on the open-access MRE platform <https://bioqic-apps.charite.de>. To test our method, we used numerical FEM simulation datasets of a box with four stiff inclusions of decreasing sizes, at excitation frequencies 50, 60, 70, 80, 90, and 100 Hz with a 1 mm isotropic resolution [2] and of an abdomen at the excitation frequencies 30, 36, 42, and 48 Hz with a 2 mm isotropic resolution [1]. We also used an *in vivo* abdomen dataset acquired at 30, 40, and 50 Hz with a $2.7 \times 2.7 \times 5$ mm³ voxel size [6] and *in vivo* kidney datasets consisting of 23 subjects acquired at 40, 50, 60, and 70 Hz and 2.5 mm isotropic resolution [13].

Implementation details. Our model was trained for 500,000 epochs on a single A-100 GPU, with training data generated on the fly using a batch size of 2048. The total number of training samples generated corresponds to the product of the batch size and the number of epochs. We used the Adam optimizer with a learning rate of 0.0001. We implemented the code using the PyTorch library.

Table 1. Comparison of the RMSE (root mean square error) in m/s for LFE, k-MDEV, TWENN, ElastoNet, and MF-ElastoNet in the FEM datasets in the ROIs (regions of interest).

Dataset	ROI	Classical inversions		Neural network inversions		
		LFE	k-MDEV	TWENN	ElastoNet	MF-ElastoNet
FEM box	inclusions	1.60	0.42	0.66	0.43	0.38
	matrix	0.26	0.27	0.85	0.43	0.26
	liver	0.21	0.27	0.28	0.19	0.13
FEM abdomen	pancreas	0.39	0.38	0.42	0.34	0.27
	spleen	0.15	0.35	0.38	0.26	0.19

Baseline. We compared MF-ElastoNet with several state-of-the-art MRE wave inversion methods: the established classical inversion methods LFE [9] and k-MDEV [21] currently used in research and clinical practice, and the recent neural network-based methods TWENN [10] and ElastoNet [3]. These methods all rely on different training protocols, inference pipelines, and algorithm choices, these design differences must be considered when comparing them.

Metrics. For the FEM datasets, where a ground truth was present, we quantified the performance of the compared methods using the root mean square error (RMSE). For the *in vivo* datasets, where no ground truth was present, we assessed the mean and standard deviation of the regions of interest (ROIs).

3.2 Results

FEM datasets. The simulated wavefield, ground truth, and reconstructed SWS maps for our method compared to the baseline methods are displayed in Figure 3 for the FEM box and FEM abdomen datasets. The RMSE in the ROIs are summarized in Table 1. MF-ElastoNet achieved improved accuracy, compared to the baseline methods and particularly with respect to the single-frequency trained neural network-based methods.

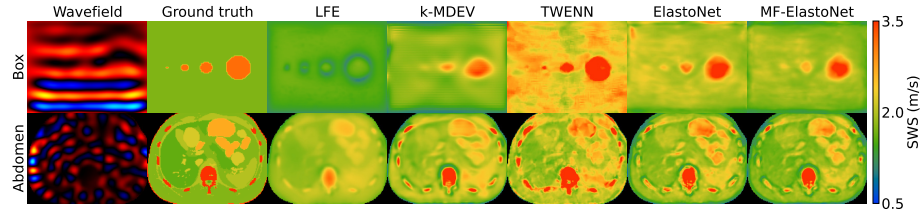


Fig. 3. Comparison of the simulated wavefield, ground truth, and predicted SWS (shear wave speed) maps produced by LFE, k-MDEV, TWENN, ElastoNet, and MF-ElastoNet for the FEM box and abdomen datasets.

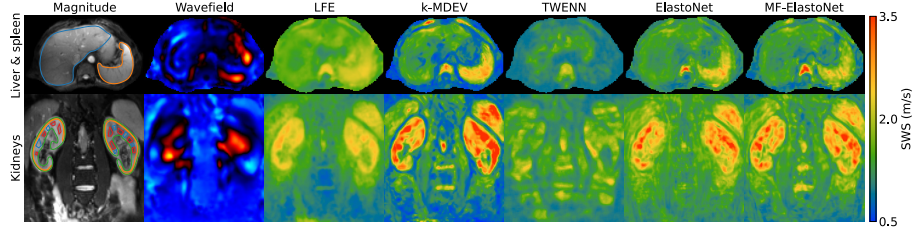


Fig. 4. Comparison of magnitude, wavefield, and predicted SWS (shear wave speed) maps produced by LFE, k-MDEV, TWENN, ElastoNet, and MF-ElastoNet for *in vivo* data: liver & spleen (liver: blue, spleen: orange) and kidneys (inner cortex: blue, medulla: red, outer cortex: orange, parenchyma: green).

Table 2. Comparison of the SWS (shear wave speed) mean \pm standard deviation in m/s of LFE, k-MDEV, TWENN, ElastoNet, and MF-ElastoNet for the *in vivo* abdomen datasets in the ROIs (regions of interest).

Dataset	ROI	Classical inversions		Neural network inversions		
		LFE	k-MDEV	TWENN	ElastoNet	MF-ElastoNet
Liver & spleen	liver	1.54 ± 0.15	1.33 ± 0.30	1.25 ± 0.22	1.37 ± 0.18	1.36 ± 0.20
	spleen	2.02 ± 0.17	2.01 ± 0.49	1.10 ± 0.13	1.90 ± 0.36	1.87 ± 0.30
Kidneys	inner cortex	1.24 ± 0.07	1.91 ± 0.16	0.87 ± 0.10	1.70 ± 0.11	1.69 ± 0.16
	medulla	1.19 ± 0.07	1.52 ± 0.17	0.92 ± 0.11	1.49 ± 0.13	1.40 ± 0.10
	outer cortex	1.09 ± 0.07	1.49 ± 0.13	0.90 ± 0.11	1.17 ± 0.08	1.35 ± 0.08
	parenchyma	1.17 ± 0.06	1.56 ± 0.14	0.92 ± 0.12	1.40 ± 0.11	1.44 ± 0.11

***In vivo* datasets.** The acquired magnitude and wavefield images, as well as the reconstructed SWS maps for our method compared to the baseline methods, are displayed in Figure 4 for the *in vivo* datasets. MF-ElastoNet showed qualitatively good anatomical detail in the reconstructed SWS maps comparable to established classical inversion methods LFE and k-MDEV. Table 2 reports the mean \pm standard deviation of the liver and spleen across the ROI in the liver & spleen dataset and the inner cortex, outer cortex, medulla, and parenchyma of the kidneys across subjects in the kidneys dataset.

Ablation study. We performed an ablation study to demonstrate the effectiveness of multifrequency training, maintaining all other training parameters unchanged. In Table 3, we report the RMSE for multifrequency training and single-frequency training with a posteriori combination for the FEM datasets. The multifrequency combination yielded a lower RMSE in the FEM datasets.

4 Discussion and Conclusion

In this paper, we proposed a fully multifrequency neural network-based wave inversion method for MRE (MF-ElastoNet). The learned multifrequency combi-

Table 3. Ablation study on multifrequency training. RMSE (root mean square error) in m/s in the FEM datasets in the ROIs (regions of interest).

Dataset	FEM box		FEM abdomen		
ROI	inclusions	matrix	liver	pancreas	spleen
Single-frequency	0.38	0.38	0.15	0.29	0.19
Multifrequency	0.38	0.34	0.13	0.27	0.19

nation stabilizes the inversion, showing increased accuracy and good anatomical detail compared to single-frequency neural network-based inversions [10,3] and established classical inversion methods [9,21]. Being flexible in terms of acquisition frequencies and resolution, it is designed to be suitable irrespective of the MRE protocol. While our method focuses on SWS reconstruction, further developments may include the calculation of other mechanical parameters, such as the penetration rate, the incorporation of heterogeneity within training patches, and uncertainty quantification. MF-ElastoNet expands on existing neural network-based inversion methods toward their use in research and clinical applications.

Acknowledgments. This work was supported by the German Research Foundation (CRC1340 Matrix in Vision, GRK2260 BIOQIC, FOR5628).

Disclosure of Interests. The authors have no competing interests to declare that are relevant to the content of this article.

References

1. Ariyurek, C., Tasdelen, B., Ider, Y.Z., Atalar, E.: SNR Weighting for Shear Wave Speed Reconstruction in Tomoelastography. *NMR in Biomedicine*. **34** (2020). <https://doi.org/10.1002/nbm.4413>
2. Barnhill, E., Davies, P.J., Ariyurek, C., Fehlner, A., Braun, J., Sack, I.: Heterogeneous Multifrequency Direct Inversion (HMDI) for magnetic resonance elastography with application to a clinical brain exam. *Medical Image Analysis*. **46**, 180–188 (2018). <https://doi.org/10.1016/j.media.2018.03.003>
3. Bustin, H., Meyer, T., Reiter, R., Jordan, J., Walczak, L., Tzschätzsch, H., Sack, I., Hennemuth, A.: ElastoNet: Neural network-based multicomponent MR elastography wave inversion with uncertainty quantification. *Medical Image Analysis*. **105**, 103642 (Oct 2025). <https://doi.org/10.1016/j.media.2025.103642>
4. Doyley, M.M.: Model-based elastography: a survey of approaches to the inverse elasticity problem. *Physics in Medicine and Biology*. **57**, R35–R73 (2012). <https://doi.org/10.1088/0031-9155/57/3/R35>
5. Fovargue, D., Nordsletten, D., Sinkus, R.: Stiffness reconstruction methods for MR elastography. *NMR in Biomedicine*. **31**, e3935 (2018). <https://doi.org/10.1002/nbm.3935>
6. Guo, J., Hirsch, S., Streitberger, K., Kamphues, C., Asbach, P., Braun, J., Sack, I.: Patient-Activated Three-Dimensional Multifrequency Magnetic Resonance Elastography for High-Resolution Mechanical Imaging of the Liver and Spleen. *RöFo - Fortschritte auf dem Gebiet der Röntgenstrahlen und der bildgebenden Verfahren*. **186**(03), 260–266 (Sep 2013). <https://doi.org/10.1055/s-0033-1350510>

7. Hirsch, S., Guo, J., Reiter, R., Papazoglou, S., Kroencke, T., Braun, J., Sack, I.: MR Elastography of the Liver and the Spleen Using a Piezoelectric Driver, Single-Shot Wave-Field Acquisition, and Multifrequency Dual Parameter Reconstruction. *Magnetic Resonance in Medicine*. **71**, 267–277 (2013). <https://doi.org/10.1002/mrm.24674>
8. Kamyab, S., Azimifar, Z., Sabzi, R., Fieguth, P.: Deep learning methods for inverse problems. *PeerJ Computer Science*. **8**, e951 (May 2022). <https://doi.org/10.7717/peerj-cs.951>
9. Knutsson, H., Westin, C.F., Granlund, G.: Local multiscale frequency and bandwidth estimation. In: *Proceedings of 1st International Conference on Image Processing. ICIP-94*, IEEE Comput. Soc. Press (1994). <https://doi.org/10.1109/icip.1994.413270>
10. Ma, S., Wang, R., Qiu, S., Li, R., Yue, Q., Sun, Q., Chen, L., Yan, F., Yang, G.Z., Feng, Y.: MR Elastography With Optimization-Based Phase Unwrapping and Traveling Wave Expansion-Based Neural Network (TWENN). *IEEE Transactions on Medical Imaging*. **42**, 2631–2642 (2023). <https://doi.org/10.1109/tmi.2023.3261346>
11. Mariappan, Y.K., Glaser, K.J., Ehman, R.L.: Magnetic resonance elastography: A review. *Clinical Anatomy*. **23**(5), 497–511 (Jun 2010). <https://doi.org/10.1002/ca.21006>
12. Meyer, T., Castelein, J., Schattenfroh, J., Sophie Morr, A., Vieira da Silva, R., Tzschätzsch, H., Reiter, R., Guo, J., Sack, I.: Magnetic resonance elastography in a nutshell: Tomographic imaging of soft tissue viscoelasticity for detecting and staging disease with a focus on inflammation. *Progress in Nuclear Magnetic Resonance Spectroscopy*. **144–145**, 1–14 (Nov 2024). <https://doi.org/10.1016/j.pnmrs.2024.05.002>
13. Meyer, T., Marticorena Garcia, S., Tzschätzsch, H., Herthum, H., Shahryari, M., Stencel, L., Braun, J., Kalra, P., Kolipaka, A., Sack, I.: Comparison of inversion methods in MR elastography: An open-access pipeline for processing multifrequency shear-wave data and demonstration in a phantom, human kidneys, and brain. *Magnetic Resonance in Medicine*. **88**, 1840–1850 (2022). <https://doi.org/10.1002/mrm.29320>
14. Morisaka, H., Motosugi, U., Ichikawa, S., Nakazawa, T., Kondo, T., Funayama, S., Matsuda, M., Ichikawa, T., Onishi, H.: Magnetic resonance elastography is as accurate as liver biopsy for liver fibrosis staging. *Journal of Magnetic Resonance Imaging*. **47**, 1268–1275 (2017). <https://doi.org/10.1002/jmri.25868>
15. Murphy, M.C., Manduca, A., Trzasko, J.D., Glaser, K.J., Huston, J., Ehman, R.L.: Artificial neural networks for stiffness estimation in magnetic resonance elastography. *Magnetic Resonance in Medicine*. **80**, 351–360 (2017). <https://doi.org/10.1002/mrm.27019>
16. Ragoza, M., Batmanghelich, K.: *Physics-Informed Neural Networks for Tissue Elasticity Reconstruction in Magnetic Resonance Elastography*, pp. 333–343. Springer Nature Switzerland (2023). https://doi.org/10.1007/978-3-031-43999-5_32
17. Sack, I.: Magnetic resonance elastography from fundamental soft-tissue mechanics to diagnostic imaging. *Nature Reviews Physics*. **5**, 25–42 (2022). <https://doi.org/10.1038/s42254-022-00543-2>
18. Sack, I., Jöhrens, K., Würfel, J., Braun, J.: Structure-sensitive elastography: on the viscoelastic powerlaw behavior of in vivo human tissue in health and disease. *Soft Matter*. **9**(24), 5672 (2013). <https://doi.org/10.1039/c3sm50552a>

19. Scott, J.M., Arani, A., Manduca, A., McGee, K.P., Trzasko, J.D., Huston, J., Ehman, R.L., Murphy, M.C.: Artificial neural networks for magnetic resonance elastography stiffness estimation in inhomogeneous materials. *Medical Image Analysis*. **63**, 101710 (2020). <https://doi.org/10.1016/j.media.2020.101710>
20. Scott, J.M., Pavuluri, K., Trzasko, J.D., Manduca, A., Senjem, M.L., Huston, J., Ehman, R.L., Murphy, M.C.: Impact of material homogeneity assumption on cortical stiffness estimates by MR elastography. *Magnetic Resonance in Medicine*. **88**, 916–929 (2022). <https://doi.org/10.1002/mrm.29226>
21. Tzschätzsch, H., Guo, J., Dittmann, F., Hirsch, S., Barnhill, E., Jöhrens, K., Braun, J., Sack, I.: Tomoelastography by multifrequency wave number recovery from time-harmonic propagating shear waves. *Medical Image Analysis*. **30**, 1–10 (May 2016). <https://doi.org/10.1016/j.media.2016.01.001>